

The spin Nernst effect in Tungsten

Peng Sheng¹, Yuya Sakuraba¹, Yong-Chang Lau^{1,2}, Saburo Takahashi³, Seiji Mitani¹ and Masamitsu Hayashi^{1,2*}

¹*National Institute for Materials Science, Tsukuba 305-0047, Japan*

²*Department of Physics, The University of Tokyo, Bunkyo, Tokyo 113-0033, Japan*

³*Institute for Materials Research, Tohoku University, Sendai 980-8577, Japan*

The spin Hall effect allows generation of spin current when charge current is passed along materials with large spin orbit coupling. It has been recently predicted that heat current in a non-magnetic metal can be converted into spin current via a process referred to as the spin Nernst effect. Here we report the observation of the spin Nernst effect in W. In W/CoFeB/MgO heterostructures, we find changes in the longitudinal and transverse voltages with magnetic field when temperature gradient is applied across the film. The field-dependence of the voltage resembles that of the spin Hall magnetoresistance. A comparison of the temperature gradient induced voltage and the spin Hall magnetoresistance allows direct estimation of the spin Nernst angle. We find the spin Nernst angle of W to be similar in magnitude but opposite in sign with its spin Hall angle. Interestingly, under an open circuit condition, such sign difference results in spin current generation larger than otherwise. These results highlight the distinct characteristics of the spin Nernst and spin Hall effects, providing pathways to explore materials with unique band structures that may generate large spin current with high efficiency.

*Email: hayashi@phys.s.u-tokyo.ac.jp

INTRODUCTION

The giant spin Hall effect(1) (SHE) in heavy metals (HM) with large spin orbit coupling has attracted great interest owing to its potential use as a spin current source to manipulate magnetization of magnetic layers(2-4). Recently it has been reported(5, 6) that the spin Hall conductivity of $5d$ transition metals depends on the number of $5d$ electrons, indicating that the observed SHE is due to the topology and filling of the characteristic bands at the Fermi surface(7, 8). Spin current in solids can be produced not only by charge current but also by heat current(9). Understanding the coupling between spin current and heat current is the central subject of Spin caloritronics(10). It is now well understood that a temperature gradient applied across a magnetic material, typically a magnetic insulator, results in spin accumulation that can be used to generate spin current in neighboring non-magnetic materials via the spin Seebeck effect(11-17).

It has been predicted theoretically(18-23) that in non-magnetic materials with strong spin orbit coupling, the heat current can be converted into spin current. The effect, often referred to as the spin Nernst effect, generates spin current that scales with the energy derivative of the spin Hall conductivity. Here we show direct probe of the spin Nernst effect in amorphous-like W, which possesses the largest spin Hall angle among the $5d$ transition metals(6, 24, 25). When an in-plane temperature gradient is applied across W/CoFeB/MgO heterostructures, we observe longitudinal and transverse voltages that vary with the magnetic field similar to those of the spin Hall magnetoresistance(26-31). The W layer thickness dependence of the longitudinal voltage is compared to that of the spin Hall magnetoresistance to estimate the size and sign of the spin Nernst angle. We

find the spin Nernst angle of W is slightly smaller than (~70%) its spin Hall angle and the two angles possess opposite sign.

RESULTS

The film structure used is sub. $|d_N$ HM $|$ 1 FM $|$ 2 MgO $|$ 1 Ta (thickness in units of nanometer), where HM is Ta or W and the ferromagnetic metal (FM) is $\text{Co}_{20}\text{Fe}_{60}\text{B}_{20}$ (referred to as CoFeB hereafter). We first study the electrical transport properties of the films. The inverse of the device longitudinal resistance ($1/R_{XX}$) multiplied by a geometrical factor (L/w), i.e. the sheet conductance (G_{XX}), is plotted as a function of the HM layer thickness (d_N) in Figs. 1(a) and 1(b) for the Ta and W underlayer films, respectively. (See inset of Fig. 1(a) for the definitions of L and w as well as the coordinate system.) We fit the data with a linear function to estimate the resistivity (ρ_N) of the HM layer. The fitting results are shown by the blue solid lines: we obtain $\rho_N \sim 183 \mu\Omega\text{cm}$ for Ta and $\sim 130 \mu\Omega\text{cm}$ for W. Note that W undergoes a structural phase transition(6, 24, 32) when its thickness is larger than ~ 6 nm, as indicated by the change in $G_{XX}=L/(wR_{XX})$ at this thickness. The spin Hall magnetoresistance (SMR), $R_{\text{SMR}}=\Delta R_{XX}/R_{XX}^Z$, is plotted as a function of the HM layer thickness in Figs. 1(c) and 1(d). We define ΔR_{XX} as the resistance difference when the magnetization of the CoFeB layer is pointing along y (R_{XX}^Y) and z (R_{XX}^Z) directions, i.e. $\Delta R_{XX}=R_{XX}^Y-R_{XX}^Z$. The thickness dependence of R_{SMR} is consistent with previous reports(6, 31).

The transverse resistance of the films is shown in Fig. 2 (see the inset of Fig. 1(a) for the details of the measurement setup). The inset of Fig. 2(a) shows the transverse

resistance (R_{XY}) vs. the out of plane field H_Z for a Ta underlayer film. We define $2\Delta R_{XY}$, i.e. the anomalous Hall resistance, as the difference in R_{XY} when the magnetization is pointing along $+z$ and $-z$. In Figs. 2(a) and 2(b), ΔR_{XY} is plotted as a function of HM layer thickness. ΔR_{XY} decreases with increasing d_N largely due to current shunting into the HM layer. To estimate the anomalous Hall angle, ΔR_{XY} is divided by R_{XX}^Z , multiplied by a geometric factor (L/w), and divided by a constant (x_F) that accounts for the current shunting effect into the HM layer: $x_F = \frac{t_F \rho_N}{t_F \rho_N + d_N \rho_F}$, where t_F and ρ_F are the thickness and resistivity of the FM layer, respectively. The HM layer thickness dependence of the normalized anomalous Hall coefficient $R_{AHE}/x_F = (\Delta R_{XY} L)/(R_{XX}^Z w x_F)$ is plotted in Figs. 2(c) and 2(d) for Ta and W underlayer films. We find that the normalized anomalous Hall coefficient shows a significant HM layer thickness dependence, in particular, for the W underlayer films.

We next show the thermoelectric properties of the films. Figure 3(a) shows a sketch of the setup to study the Seebeck coefficient of the films. A heater is placed near one side of the substrate to create a temperature gradient across the substrate. The difference in the temperature between the hot (T_H) and cold (T_L) sides of the substrate ($\Delta T = T_H - T_L$), across a distance D , is measured using an infrared camera. The longitudinal (Seebeck) voltage $V_{XX} = V(x_1) - V(x_2)$ is measured between two points of the device separated by a distance L ($L < D$). The temperature of position x_1 is higher than that of x_2 ; see Fig. 3(a). The ΔT dependence of V_{XX} is shown in Figs. 3(b) and 3(c) for the Ta and W underlayer films, respectively. The data is fitted with a linear function to extract the Seebeck coefficient(33) $S = -(V_{XX}/L)/(\Delta T/D)$ from the slope, which is plotted as a function of d_N in

Figs. 3(d) and 3(e). S approaches $\sim -4 \mu\text{V/K}$ when the HM layer thickness is thin for both film structures, which we consider provides information of the Seebeck coefficient of CoFeB (we assume that the MgO and the oxidized Ta capping layers have negligible contribution to V_{XX}). In contrast, the thick limit of d_N gives the Seebeck coefficient of the HM layer: we estimate $S \sim -2 \mu\text{V/K}$ for Ta and $\sim -12 \mu\text{V/K}$ for W.

The off diagonal component of the thermoelectric properties is summarized in Fig. 4. The experimental setup to study the temperature gradient induced transverse voltage is depicted in Fig. 4(a). A typical hysteresis loop obtained by measuring the H_Z dependence of the temperature gradient induced transverse voltage $V_{XY} = V_{XY}(y_2) - V_{XY}(y_1)$ (see Fig. 4(a) for the definitions of y_1 and y_2) is shown in Fig. 4(b). Similar to the anomalous Hall resistance, we define $2\Delta V_{XY}$, i.e. the anomalous Nernst voltage, as the difference in V_{XY} when the magnetization is pointing along $+z$ and $-z$. Figure 4(c) shows the ΔT dependence of ΔV_{XY} for a W underlayer film. Within the applied temperature gradient, the response is linear. We thus fit a linear function to obtain the anomalous Nernst coefficient $S_{\text{ANE}} = (\Delta V_{XY}/L)/(\Delta T/D)$ from the slope (here $L = y_2 - y_1$).

The HM layer thickness dependence of anomalous Nernst coefficient S_{ANE} is plotted for the Ta and W underlayer films in Figs. 4(d) and 4(e), respectively. $|S_{\text{ANE}}|$ decreases with increasing d_N for the Ta underlayer films whereas it shows a peak at around $d_N \sim 3$ nm for the W underlayer films. Similar to the anomalous Hall resistance, the presence of the HM layer can shunt the Hall voltage. To account for such effect, S_{ANE} is divided by x_F . The normalized anomalous Nernst coefficient S_{ANE}/x_F is plotted as a function of d_N in

Figs. 4(f) and 4(g). We find a larger variation of S_{ANE}/x_F with d_N for the W underlayer films than the Ta underlayer films.

Recent studies have shown that spin current generated within the HM layer modifies the anomalous Hall resistance via a non-zero imaginary part of the spin mixing conductance at the HM/FM interface(26, 27, 34). The large variation of the normalized anomalous Nernst coefficient with d_N for the W underlayer films indicates that a temperature gradient can cause spin current generation in the W layer that results in modification of the off diagonal component. To evaluate the temperature gradient induced spin current generation, i.e. the spin Nernst effect, in a more explicit way, we have studied the external field dependence of the Seebeck voltage in analogy to the SMR. The experimental setup is the same with that of Fig. 3(a): here a large external magnetic field is applied during the measurements.

In Figs. 5(a) and 5(b), we show the longitudinal (Seebeck) voltage $V_{XX}=V(x_1)-V(x_2)$ of Ta and W underlayer films, respectively, plotted as a function of external field directed along the y -axis (H_Y). The temperature difference ΔT across the substrate is ~ 3.5 K. For the W underlayer films (Fig. 5(b)), we find a peak-like structure around zero field. (Signals are shifted vertically for clarity so that the large field limit of V_{XX} equals zero.) The peak found in the V_{XX} vs. H_Y plot decays to zero when $|H_Y| \sim |H_K|$, where H_K is the effective anisotropy field required to force the magnetization to point along the film plane (see supplementary materials for the magnetic properties of the heterostructures). The peak amplitude ΔV_{XX} defined schematically in Fig. 5(b) is equivalent to the difference in V_{XX} when the magnetization is pointing along the y -axis (V_{XX}^Y) and the z -axis (V_{XX}^Z), i.e. $\Delta V_{XX}=V_{XX}^Y-V_{XX}^Z$. Such definition is in accordance to that of SMR. We have also studied

V_{XX} as a function of H_X and H_Z : the results are shown in the supplementary material (Fig. S2). In contrast to V_{XX} vs. H_Y , we find no clear feature in the H_X and H_Z dependence of V_{XX} . These results suggest that the thermal analogue of the anisotropic magnetoresistance (AMR) is small in CoFeB(35). Note that the AMR of the CoFeB layer here is $\sim 0.1\%$ (31), much smaller than that of the Ni-based soft magnetic materials(36). The small temperature gradient induced AMR-like voltage (V_{XX} vs. H_X , see Fig. S2) found here also indicates that possible contribution from combination of AMR and interfacial spin orbit coupling(37, 38) on ΔV_{XX} may be small. We also find little of evidence of proximity induced magnetism(39-41) in W and Ta, which may influence the temperature gradient induced voltage via AMR in the HM layer.

In Fig. 5(c), we plot $S_{SNE}=(\Delta V_{XX}/L)/(\Delta T/D)$, which we refer to as the spin Nernst coefficient, as a function of the W layer thickness. Interestingly $|S_{SNE}|$ takes a maximum at $d_N \sim 3-4$ nm, similar to that of the SMR shown in Fig. 1(d). These results indicate that the interfacial magnetoresistance caused by the Rashba interaction, which takes a maximum at a HM layer thickness close to one lattice constant(42), is not the main source of the voltage (S_{SNE}) found here. See supplementary material (Figs. S3 and S4) for discussions on the effects of the FM layer (CoFeB) and an unintended out of plane temperature gradient(15, 43-45) on the voltage measurements.

To account for these results, a drift-diffusion model is extended to describe spin transport in a bilayer system. The HM layer thickness dependence of the SMR and the anomalous Hall coefficient are described with the following equations(26, 31):

$$R_{SMR} \equiv \frac{\Delta R_{XX}}{R_{XX}^Z} = -(1-x_F)\theta_{SH}^2 \frac{\lambda_N}{d_N} \tanh^2\left(\frac{d_N}{2\lambda_N}\right) \text{Re}\left[\frac{g_S}{1+g_S \coth(d_N/\lambda_N)}\right] \quad (1)$$

$$R_{\text{AHE}} \equiv \frac{\Delta R_{\text{XY}}}{R_{\text{XX}}} \frac{L}{w} = -x_F \theta_{\text{AH}} + (1-x_F) \theta_{\text{SH}}^2 \frac{\lambda_N}{d_N} \tanh^2\left(\frac{d_N}{2\lambda_N}\right) \text{Im} \left[\frac{g_S}{1+g_S \coth(d_N/\lambda_N)} \right] \quad (2)$$

where θ_{SH} and λ_N are the spin Hall angle and the spin diffusion length of the HM layer, θ_{AH} is the anomalous Hall angle of the FM layer. $g_S = 2\rho_N \lambda_N G_{\text{MIX}}$, where G_{MIX} is the spin mixing conductance of the HM/FM interface. Here for simplicity we have neglected contribution of longitudinal spin current absorption on the SMR(31).

Furthermore, we assume that a temperature gradient (∇T) applied across a sample can generate spin current \mathbf{Q} (i.e. flow of spin-angular momentum carried by electrons) via the spin Nernst effect in a similar way an electric field \mathbf{E} (or current) generates spin current through the spin Hall effect, i.e.

$$Q_{kj} = \frac{\hbar}{2|e|} \theta_{\text{SH}} \left(\mathbf{e}_k \times \frac{\mathbf{E}}{\rho_N} \right) \Big|_j + \frac{\hbar}{2|e|} \theta_{\text{SN}} \left(\mathbf{e}_k \times \frac{S_N}{\rho_N} (-\nabla T) \right) \Big|_j \quad (3)$$

Indices k and j denote, respectively, the spin and flow direction of the spin current (\mathbf{e}_k is an unit vector.) \hbar is the reduced Planck constant, e is the electron's charge. S_N and θ_{SN} are the Seebeck coefficient and the spin Nernst angle of the HM layer, respectively. For simplicity, we do not consider the spin Hall and spin Nernst effects of the FM layer since θ_{SH} of FM has been reported to be small compared to that of the HM layers(46-48). In the FM layer, however, the anomalous Hall and the anomalous Nernst effects generate a transverse charge current \mathbf{J}^T when \mathbf{E} and ∇T are applied. The transverse charge current (opposite to the electron flow) is:

$$J_j^T = -\theta_{\text{AH}} \left(\mathbf{m} \times \frac{\mathbf{E}}{\rho_F} \right) \Big|_j - \theta_{\text{AN}} \left(\mathbf{m} \times \frac{S_F}{\rho_F} (-\nabla T) \right) \Big|_j \quad (4)$$

where \hat{m} is an unit vector representing the magnetization direction of the FM layer. S_F and θ_{AN} are the Seebeck coefficient and the anomalous Nernst angle of the FM layer, respectively.

We assume a temperature gradient $\frac{\Delta T}{D} = \frac{T_H - T_L}{D}$ is applied under an open circuit

condition. The change in the longitudinal voltage ($\frac{V_{XX}}{L} = \frac{V_{XX}(x_1) - V_{XX}(x_2)}{x_2 - x_1}$) when the

magnetization of the FM layer is pointing along y (V_{XX}^y) and z (V_{XX}^z) axes,

$\Delta V_{XX} = V_{XX}^y - V_{XX}^z$, is expressed as:

$$S_{SNE} \equiv \frac{\Delta V_{XX}/L}{\Delta T/D} = (1 - x_F) \theta_{SH} \{ \theta_{SH} S - \theta_{SN} S_N \} \frac{\lambda_N}{d_N} \tanh^2 \left(\frac{d_N}{2\lambda_N} \right) \text{Re} \left[\frac{g_S}{1 + g_S \coth(d_N/\lambda_N)} \right] \quad (5)$$

Similarly, the difference in the transverse voltage ($\frac{V_{XY}}{L} = \frac{V_{XY}(y_2) - V_{XY}(y_1)}{y_2 - y_1}$) when the

magnetization reverses its direction from $+z$ to $-z$, $2\Delta V_{XY} = V_{XY}^z - V_{XY}^{-z}$, reads:

$$S_{ANE} \equiv \frac{\Delta V_{XY}/L}{\Delta T/D} = x_F \{ \theta_{AH} S - \theta_{AN} S_F \} - (1 - x_F) \theta_{SH} \{ \theta_{SH} S - \theta_{SN} S_N \} \frac{\lambda_N}{d_N} \tanh^2 \left(\frac{d_N}{2\lambda_N} \right) \text{Im} \left[\frac{g_S}{1 + g_S \coth(d_N/\lambda_N)} \right] \quad (6)$$

Equations (5) and (6) represent the d_N dependence of the spin Nernst and anomalous Nernst coefficients, respectively. The Seebeck coefficient of the HM/FM bilayer, defined as $S = x_F S_F + (1 - x_F) S_N$, is obtained experimentally using the relation $S = -(V_{XX}/L)/(\Delta T/D)$ and the results are shown in Figs. 3(d,e). We note that when $\theta_{SN}=0$, $S_{SNE} = S R_{SMR}$: the functional form of S_{SNE} and R_{SMR} is the same.

The first term ($\theta_{SH}S$) in the curly bracket of Eq. (5) appears due to the open circuit condition. That is, the electrons initially move from the hot to cold side when a temperature gradient is applied (the Seebeck coefficients of the FM and HM layers are all negative). Once the electrons reach the edge of the patterned structure, an internal electric field E_{INT} develops due to charge accumulation at the edges. The direction of E_{INT} is such that it cancels the electron flow driven by the temperature gradient, resulting in a net zero current. However, spin current can be generated via the spin Hall effect when a non-zero E_{INT} exists, thus contributing to the SMR. The second term ($\theta_{SN}S_N$) in the curly bracket of Eq. (5) corresponds to contribution to the SMR that results from a direct conversion of heat current to spin current. Similar classification also applies to the terms in the curly brackets of Eq. (6).

The model calculations are compared to the experimental results presented in Figs. 1(c,d), 2(c,d), 4(f,g) and 5(c) to find a parameter set that best describes the results. The fitting results are shown by the solid lines in each figure and the parameters extracted (θ_{SH} , θ_{AH} , λ_N , θ_{SN} , θ_{AN} , $\text{Re}[G_{MIX}]$, $\text{Im}[G_{MIX}]$) are summarized in Table 1. (See the methods section for the details of the fitting process.) The spin Hall angle (θ_{SH}) estimated for Ta and W underlayers are consistent with previous reports(2, 6, 24, 25, 31). These results show that the model can account for all results shown in Figs. 1-5 using a single set of parameters listed in Table 1. Note that the spin mixing conductance obtained from the fitting is mostly consistent with previous reports (see the Materials and methods section for the details).

To illustrate the effect of the spin Nernst effect on the transport properties more clearly, the spin Nernst and anomalous Nernst coefficients are numerically calculated using Eqs. (5) and (6) with three different spin Nernst angles, $\theta_{SN}=-\theta_{SH}$, $\theta_{SN}=0$, $\theta_{SN}=\theta_{SH}$. The open circles in Fig. 5(c) represent the scaled spin Hall magnetoresistance SR_{SMR} calculated using the results of Figs. 1(d) and 3(e). As described above, SR_{SMR} lies on the $\theta_{SN}=0$ line. This demonstrates that the internal electric field \mathbf{E}_{INT} partly contributes to the spin current generation. In contrast, the spin Nernst coefficient S_{SNE} (solid circles) lies closer to the $\theta_{SN}=-\theta_{SH}$ line. When the signs of θ_{SN} and θ_{SH} are opposite, contribution from the heat current induced spin current adds constructively to the \mathbf{E}_{INT} induced spin current. Note that for the Ta underlayer films, the expected spin Nernst coefficient using Eq. (5) and the parameters defined in Table 1 (with $\theta_{SN}=-\theta_{SH}$) is ~ 0.01 ($\mu\text{V}/\text{K}$): this is smaller than the experimental resolution and we consider this is the reason we find no characteristic feature in the voltage measurements (Fig. 5(a)).

Furthermore, we show that the spin Nernst angle θ_{SN} can be extracted just from the experimental results. From Eqs. (1) and (5), we obtain:

$$\frac{\theta_{SN}}{\theta_{SH}} = \frac{S}{S_N} \left[\frac{S_{SNE}}{SR_{SMR}} + 1 \right] \quad (7)$$

In Fig. 5(d) we plot θ_{SN}/θ_{SH} obtained by calculating $S_{SNE}/(SR_{SMR})$ using the results of Figs. 1(d), 3(e) and 5(c) (and Eq. (7)). The plot clearly shows the signs of the spin Nernst and spin Hall angles are opposite and the magnitude of the former is somewhat smaller than the latter. (Meyer *et al* have studied the spin Nernst effect in Pt/YIG and found that the signs of two angles are opposite for Pt too(49); however, the spin Nernst angle of Pt was reported to be larger than its spin Hall angle.) From numerical calculations, we find

that θ_{SN}/θ_{SH} is not susceptible to the values of the spin mixing conductance and the degree of longitudinal spin absorption (i.e. the spin polarization of the FM layer), which influences the absolute values of R_{SMR} and S_{SNE} (31). The calculations also show that θ_{SN}/θ_{SH} is not significantly influenced by contribution(s) from the anomalous Hall/anomalous Nernst effects and the spin Hall/spin Nernst effects, if any, of the FM layer as long as the HM layer thickness d_N is larger than λ_N (details will be reported elsewhere). When d_N is smaller than λ_N , these effects can influence the value of θ_{SN}/θ_{SH} : the slight increase in θ_{SN}/θ_{SH} found in Fig. 5(c) may be due to this contribution. We thus consider the large d_N limit of θ_{SN}/θ_{SH} provides a better estimate, from which we find $\theta_{SN}/\theta_{SH} \sim 0.7$.

DISCUSSION

Interestingly, the anomalous Nernst and the anomalous Hall angles(50-54) of CoFeB also possess the opposite sign (see Table 1), which results in a larger anomalous Nernst effect than otherwise. Theoretically, the sign of the Nernst and Hall angles do not necessarily have to match(33) as the Nernst angle (θ_{AN} , θ_{SN}) is defined by the energy derivative of the corresponding Hall conductivity near the Fermi energy, which can be positive or negative regardless of the sign of the Hall angle (θ_{AH} , θ_{SH}). Thus the sign as well as the magnitude of the Nernst angle can be very different from the Hall angle. The recently reported spin Hall tunneling spectroscopy(55) and/or the temperature gradient induced magnetization measurements(56) may provide access to information on the

energy level dependence of the Hall conductivity and can be used to verify the relationship between the Hall and Nernst angles.

We briefly discuss contributions from other effects that may influence the signal due to the spin Nernst effect (see Supplementary Material Table S1 for more details). It has been reported that an unintended out of plane temperature gradient may develop during the application of an in-plane temperature gradient(15, 43-45). Under such circumstance, the anomalous Nernst effect of the FM layer can contaminate the signals observed in the voltage measurements. We observe such longitudinal voltage (V_{XX}) in film structures without the HM (W) layer and thicker FM (CoFeB) layer under application of H_Y . However, the H_Y dependence of V_{XX} is distinct: the values of V_{XX} when the magnetization points along $+y$ and $-y$ are different for the anomalous Nernst voltage caused by the unintended out of plane temperature gradient (Supplementary material, Figs. S3(l-n)) whereas the values lie at the same level for the spin Nernst coefficient induced by the in-plane temperature gradient (Fig. 5(b)). For similar reason, the combined effect of the spin Seebeck effect within the FM layer and the inverse spin Hall effect of the HM layer under an out of plane temperature gradient can be excluded. The size of the unintended out of plane temperature gradient scales with the thickness of the CoFeB layer and it is smaller than the detection limit for the 1 nm thick CoFeB layer used here (see Supplemental material, Figs. S3(g-j)). We have also confirmed that the spin Nernst coefficient S_{SNE} is negligible for heterostructures without the W layer (e.g. in Sub.|1 CoFeB|2 MgO|1 Ta) (see Supplemental material, Figs. S3(k) and S3(l)).

The results presented here not only provide insights into thermoelectric generation of spin current in heavy metals with strong spin orbit coupling but also have important

implications on expanding the search of materials that can generate spin current. The spin Nernst effect may be able to generate spin current from materials that is not possible with the spin Hall effect, for example, in systems where the density of states at the Fermi level is zero. Of particular interest are the two dimensional chalcogenides and the Weyl semi metals in which the Fermi level coincides with the Dirac point. The spin Nernst effect may thus broaden material research on spin current generation beyond the current reach of the spin Hall effect.

MATERIALS AND METHODS

A. Sample preparation and measurements

All films are deposited using magnetron sputtering on non-doped silicon substrates coated with ~100 nm thick thermal oxides (SiO_x). Films are post-annealed at ~300°C for 1 hour prior to the device patterning processes. Optical lithography and Ar ion etching are used to pattern the films into wires and Hall bars. Contact pads made of 5 Ta|100 Au (unit in nanometer) are formed by a liftoff process.

All measurements are performed at room temperature. Temperature gradient across the substrate is applied by placing a ceramic heater on one side of the substrate and a heat absorbing Cu block on the other side. The substrate is fixed to the heater/Cu block using a thermally conducting double sided tape made of Al. The temperature profile of the system is studied using an infrared camera with Si substrates coated with black body matt (the surface emissivity is calibrated). The camera is used to ensure that the temperature gradient across the substrate is uniform. Due to the necessity of this coating, the

temperature profile of the device under investigation cannot be monitored in real time: once the sample is coated with the black body matt, it is difficult to perform the voltage measurements. As the temperature gradient across the substrate largely depends on the contact between the substrate and the heater/Cu block, we have checked its variation by placing the substrate to the setup multiple times and monitored the temperature profile using the infrared camera. The variation of the temperature gradient is $\sim\pm 10\%$ of the average value. The horizontal error bars in Figs. 3(b,c) and 4(c) reflect this variation. The vertical error bars in the same figures represent the distribution of the voltage when measurements are repeated multiple times under the same contact between the substrate and heater/Cu block. The vertical error bars are smaller than the symbols, suggesting that the measurements are stable and the temperature gradient do not evolve once the substrate is fixed. Thus the dominant source of the measurement error originates from the uncertainty in the actual value of the temperature gradient across the substrate: the error bars in Figs. 3(d,e), 4(d-g) and 5(c,d) reflect this uncertainty.

B. Fitting procedure

Experimental results are fitted using Eqs. (1,2,5,6). Before carrying out the fitting, we determine the following parameters from the experimental results. The resistivity (ρ_N) of the HM layers are obtained by the d_N dependence of G_{XX} shown in Figs. 1(a,b). For the resistivity (ρ_F) of the FM (CoFeB) layer, we use a value from our previous studies(57). The Seebeck coefficients of the HM layer (S_N) and the FM layer (S_F) are estimated from the results presented in Figs. 3(d,e). We have also measured the Seebeck coefficient of

the FM layer (S_F) independently using a film stack that does not include any HM layer: results are shown in Fig. S4(i). We find that S_F estimated from film stacks with and without the HM layer are similar. The anomalous Hall angle (θ_{AH}) and the anomalous Nernst angle (θ_{AN}) of the FM (CoFeB) layer can be estimated by the zero HM thickness limit of the normalized R_{AHE} (Figs. 2(c,d)) and the normalized S_{ANE} (Figs. 4(f,g)), respectively.

We first fit R_{SMR} (Figs. 1(c,d)) and R_{AHE} (Figs. 2(c,d)) using Eqs. (1) and (2) to determine θ_{SH} , λ_N , $\text{Re}[G_{MIX}]$ and $\text{Im}[G_{MIX}]$. Note that in many previous studies, a transparent interface ($\text{Re}[G_{MIX}] \gg \text{Im}[G_{MIX}]$ and $\text{Re}[G_{MIX}] \gg 1/(2\rho_N\lambda_N)$) has been assumed to estimate the lower bound of θ_{SH} . In such case, G_{MIX} drops off from Eq. (1) and simplifies the fitting. Here we use $\text{Re}[G_{MIX}]$ and $\text{Im}[G_{MIX}]$ as the fitting parameters to account for the d_N dependence of R_{SMR} and R_{AHE} . For both underlayer films, we find that $\text{Im}[G_{MIX}]$ has to be negative and larger in magnitude than $\text{Re}[G_{MIX}]$. Such characteristic G_{MIX} is in agreement with the current induced torque found in similar heterostructures(58-60) according to the relation of G_{MIX} and the torque(61). For the Ta underlayer films, the change in R_{AHE} with d_N is larger than what is expected from Eq. (2). As the anomalous Hall effect is known to be susceptible to interface states(62, 63), we infer that there are other effects that are not captured by Eq. (2).

Using these numbers (θ_{SH} , λ_N , $\text{Re}[G_{MIX}]$ and $\text{Im}[G_{MIX}]$), S_{SNE} (Fig. 5(c)) and S_{ANE} (Figs. 4(f,g)) are calculated using Eqs. (5) and (6) with θ_{SN} denoted in the legend of each figure.

SUPPLEMENTARY MATERIALS

Supplementary material for this article is available.

Fig. S1. Magnetic properties of HM/CoFeB/MgO heterostructures.

Fig. S2. Spin Nernst magnetoresistance of Ta and W underlayer films.

Fig. S3. Thermoelectric properties of CoFeB thin films without HM layer.

Fig. S4. Comparison of parameters with and without the HM layer.

Table S1. Influence of other phenomena on the temperature gradient induced voltage measurements.

REFERENCES AND NOTES

1. M. I. Dyakonov, V. I. Perel, Current-Induced Spin Orientation of Electrons in Semiconductors. *Phys. Lett. A* **35**, 459 (1971).
2. L. Liu, C.-F. Pai, Y. Li, H. W. Tseng, D. C. Ralph, R. A. Buhrman, Spin-Torque Switching with the Giant Spin Hall Effect of Tantalum. *Science* **336**, 555 (2012).
3. A. Hoffmann, Spin Hall Effects in Metals. *IEEE Trans. Magn.* **49**, 5172 (2013).
4. T. Jungwirth, J. Wunderlich, K. Olejnik, Spin Hall effect devices. *Nat. Mater.* **11**, 382 (2012).
5. M. Morota, Y. Niimi, K. Ohnishi, D. H. Wei, T. Tanaka, H. Kontani, T. Kimura, Y. Otani, Indication of intrinsic spin Hall effect in 4d and 5d transition metals. *Phys. Rev. B* **83**, 174405 (2011).
6. J. Liu, T. Ohkubo, S. Mitani, K. Hono, M. Hayashi, Correlation between the spin Hall angle and the structural phases of early 5d transition metals. *Appl. Phys. Lett.* **107**, 232408 (2015).
7. G. Y. Guo, S. Murakami, T. W. Chen, N. Nagaosa, Intrinsic Spin Hall Effect in Platinum: First-Principles Calculations. *Phys. Rev. Lett.* **100**, 096401 (2008).
8. T. Tanaka, H. Kontani, M. Naito, T. Naito, D. S. Hirashima, K. Yamada, J. Inoue, Intrinsic spin Hall effect and orbital Hall effect in 4d and 5d transition metals. *Phys. Rev. B* **77**, 165117 (2008).
9. K. Uchida, S. Takahashi, K. Harii, J. Ieda, W. Koshibae, K. Ando, S. Maekawa, E. Saitoh, Observation of the spin Seebeck effect. *Nature* **455**, 778 (2008).
10. G. E. W. Bauer, E. Saitoh, B. J. van Wees, Spin caloritronics. *Nat. Mater.* **11**, 391 (2012).
11. J. Xiao, G. E. W. Bauer, K.-c. Uchida, E. Saitoh, S. Maekawa, Theory of magnon-driven spin Seebeck effect. *Phys. Rev. B* **81**, 214418 (2010).
12. K. Uchida, J. Xiao, H. Adachi, J. Ohe, S. Takahashi, J. Ieda, T. Ota, Y. Kajiwara, H. Umezawa, H. Kawai, G. E. W. Bauer, S. Maekawa, E. Saitoh, Spin Seebeck insulator. *Nat. Mater.* **9**, 894 (2010).
13. C. M. Jaworski, J. Yang, S. Mack, D. D. Awschalom, J. P. Heremans, R. C. Myers, Observation of the spin-Seebeck effect in a ferromagnetic semiconductor. *Nat Mater* **9**, 898 (2010).
14. A. Slachter, F. L. Bakker, J. P. Adam, B. J. van Wees, Thermally driven spin injection from a ferromagnet into a non-magnetic metal. *Nat. Phys.* **6**, 879 (2010).
15. S. Y. Huang, W. G. Wang, S. F. Lee, J. Kwo, C. L. Chien, Intrinsic Spin-Dependent Thermal Transport. *Phys. Rev. Lett.* **107**, 216604 (2011).
16. G. M. Choi, C. H. Moon, B. C. Min, K. J. Lee, D. G. Cahill, Thermal spin-transfer torque driven by the spin-dependent Seebeck effect in metallic spin-valves. *Nat. Phys.* **11**, 576 (2015).
17. L. J. Cornelissen, J. Liu, R. A. Duine, J. Ben Youssef, B. J. van Wees, Long-distance transport of magnon spin information in a magnetic insulator at room temperature. *Nat. Phys.* **11**, 1022 (2015).
18. S.-g. Cheng, Y. Xing, Q.-f. Sun, X. C. Xie, Spin Nernst effect and Nernst effect in two-dimensional electron systems. *Phys. Rev. B* **78**, 045302 (2008).
19. Z. Ma, Spin Hall effect generated by a temperature gradient and heat current in a two-dimensional electron gas. *Solid State Commun.* **150**, 510 (2010).
20. K. Tauber, M. Gradhand, D. V. Fedorov, I. Mertig, Extrinsic Spin Nernst Effect from First Principles. *Phys. Rev. Lett.* **109**, 026601 (2012).
21. S. Wimmer, D. Koedderitzsch, K. Chadova, H. Ebert, First-principles linear response description of the spin Nernst effect. *Phys. Rev. B* **88**, 201108 (2013).
22. G. Geranton, F. Freimuth, S. Bluegel, Y. Mokrousov, Spin-orbit torques in L1(0)-FePt/Pt thin films driven by electrical and thermal currents. *Phys. Rev. B* **91**, 014417 (2015).

23. K. Tauber, D. V. Fedorov, M. Gradhand, I. Mertig, Spin Hall and spin Nernst effect in dilute ternary alloys. *Phys. Rev. B* **87**, 161114 (2013).
24. C. F. Pai, L. Q. Liu, Y. Li, H. W. Tseng, D. C. Ralph, R. A. Buhrman, Spin transfer torque devices utilizing the giant spin Hall effect of tungsten. *Appl. Phys. Lett.* **101**, 122404 (2012).
25. Q. Hao, W. Z. Chen, G. Xiao, Beta (beta) tungsten thin films: Structure, electron transport, and giant spin Hall effect. *Appl. Phys. Lett.* **106**, 182403 (2015).
26. Y. T. Chen, S. Takahashi, H. Nakayama, M. Althammer, S. T. B. Goennenwein, E. Saitoh, G. E. W. Bauer, Theory of spin Hall magnetoresistance. *Phys. Rev. B* **87**, 144411 (2013).
27. H. Nakayama, M. Althammer, Y. T. Chen, K. Uchida, Y. Kajiwara, D. Kikuchi, T. Ohtani, S. Geprags, M. Opel, S. Takahashi, R. Gross, G. E. W. Bauer, S. T. B. Goennenwein, E. Saitoh, Spin Hall Magnetoresistance Induced by a Nonequilibrium Proximity Effect. *Phys. Rev. Lett.* **110**, 206601 (2013).
28. M. Althammer, S. Meyer, H. Nakayama, M. Schreier, S. Altmannshofer, M. Weiler, H. Huebl, S. Gepraegs, M. Opel, R. Gross, D. Meier, C. Klewe, T. Kuschel, J.-M. Schmalhorst, G. Reiss, L. Shen, A. Gupta, Y.-T. Chen, G. E. W. Bauer, E. Saitoh, S. T. B. Goennenwein, Quantitative study of the spin Hall magnetoresistance in ferromagnetic insulator/normal metal hybrids. *Phys. Rev. B* **87**, 224401 (2013).
29. C. Hahn, G. de Loubens, O. Klein, M. Viret, V. V. Naletov, J. Ben Youssef, Comparative measurements of inverse spin Hall effects and magnetoresistance in YIG/Pt and YIG/Ta. *Phys. Rev. B* **87**, 174417 (2013).
30. C. O. Avci, K. Garello, A. Ghosh, M. Gabureac, S. F. Alvarado, P. Gambardella, Unidirectional spin Hall magnetoresistance in ferromagnet/normal metal bilayers. *Nat. Phys.* **11**, 570 (2015).
31. J. Kim, P. Sheng, S. Takahashi, S. Mitani, M. Hayashi, Spin Hall Magnetoresistance in Metallic Bilayers. *Phys. Rev. Lett.* **116**, 097201 (2016).
32. S. M. Rossnagel, I. C. Noyan, C. Cabral, Phase transformation of thin sputter-deposited tungsten films at room temperature. *J. Vac. Sci. Technol. B* **20**, 2047 (2002).
33. N. F. Mott, G. H. Jones, *The Theory of the Properties of Metals and Alloys*. (Dover Publications, 1958).
34. S. Meyer, R. Schlitz, S. Gepraegs, M. Opel, H. Huebl, R. Gross, S. T. B. Goennenwein, Anomalous Hall effect in YIG vertical bar Pt bilayers. *Appl. Phys. Lett.* **106**, 132402 (2015).
35. P. Krzysteczko, X. K. Hu, N. Liebing, S. Sievers, H. W. Schumacher, Domain wall magneto-Seebeck effect. *Phys. Rev. B* **92**, 140405 (2015).
36. T. R. McGuire, R. I. Potter, Anisotropic Magnetoresistance in Ferromagnetic 3d Alloys. *IEEE Trans. Magn.* **11**, 1018 (1975).
37. A. Kobs, S. Hesse, W. Kreuzpaintner, G. Winkler, D. Lott, P. Weinberger, A. Schreyer, H. P. Oepen, Anisotropic Interface Magnetoresistance in Pt/Co/Pt Sandwiches. *Phys. Rev. Lett.* **106**, 217207 (2011).
38. S. S. L. Zhang, S. F. Zhang, Angular dependence of anisotropic magnetoresistance in magnetic systems. *J. Appl. Phys.* **115**, 17c703 (2014).
39. Y. M. Lu, J. W. Cai, S. Y. Huang, D. Qu, B. F. Miao, C. L. Chien, Hybrid magnetoresistance in the proximity of a ferromagnet. *Phys. Rev. B* **87**, 220409 (2013).
40. J. X. Li, M. W. Jia, Z. Ding, J. H. Liang, Y. M. Luo, Y. Z. Wu, Pt-enhanced anisotropic magnetoresistance in Pt/Fe bilayers. *Phys. Rev. B* **90**, 214415 (2014).
41. T. Kikkawa, K. Uchida, S. Daimon, Y. Shiomi, H. Adachi, Z. Qiu, D. Hou, X. F. Jin, S. Maekawa, E. Saitoh, Separation of longitudinal spin Seebeck effect from anomalous Nernst effect: Determination of origin of transverse thermoelectric voltage in metal/insulator junctions. *Phys. Rev. B* **88**, 214403 (2013).

42. V. L. Grigoryan, W. Guo, G. E. W. Bauer, J. Xiao, Intrinsic magnetoresistance in metal films on ferromagnetic insulators. *Phys. Rev. B* **90**, 161412 (2014).
43. S. Bosu, Y. Sakuraba, K. Uchida, K. Saito, T. Ota, E. Saitoh, K. Takanashi, Spin Seebeck effect in thin films of the Heusler compound Co₂MnSi. *Phys. Rev. B* **83**, 224401 (2011).
44. D. Meier, D. Reinhardt, M. Schmid, C. H. Back, J. M. Schmalhorst, T. Kuschel, G. Reiss, Influence of heat flow directions on Nernst effects in Py/Pt bilayers. *Phys. Rev. B* **88**, 184425 (2013).
45. M. Schmid, S. Srichandan, D. Meier, T. Kuschel, J. M. Schmalhorst, M. Vogel, G. Reiss, C. Strunk, C. H. Back, Transverse Spin Seebeck Effect versus Anomalous and Planar Nernst Effects in Permalloy Thin Films. *Phys. Rev. Lett.* **111**, 187201 (2013).
46. B. F. Miao, S. Y. Huang, D. Qu, C. L. Chien, Inverse Spin Hall Effect in a Ferromagnetic Metal. *Phys. Rev. Lett.* **111**, 066602 (2013).
47. A. Tsukahara, Y. Ando, Y. Kitamura, H. Emoto, E. Shikoh, M. P. Delmo, T. Shinjo, M. Shiraishi, Self-induced inverse spin Hall effect in permalloy at room temperature. *Phys. Rev. B* **89**, 235317 (2014).
48. J. Cramer, F. Fuhrmann, U. Ritzmann, V. Gall, T. Niizeki, R. Ramos, Z. Qiu, D. Hou, T. Kikkawa, J. Sinova, U. Nowak, E. Saitoh, M. Kläui, Ferroic collinear multilayer magnon spin valve. arXiv:1706.07592.
49. S. Meyer, Y.-T. Chen, S. Wimmer, M. Althammer, S. Geprägs, H. Huebl, D. Ködderitzsch, H. Ebert, G. E. W. Bauer, R. Gross, S. T. B. Goennenwein, Observation of the spin Nernst effect. arXiv:1607.02277 (2016).
50. T. Miyasato, N. Abe, T. Fujii, A. Asamitsu, S. Onoda, Y. Onose, N. Nagaosa, Y. Tokura, Crossover behavior of the anomalous hall effect and anomalous nernst effect in itinerant ferromagnets. *Phys. Rev. Lett.* **99**, 086602 (2007).
51. Y. Pu, D. Chiba, F. Matsukura, H. Ohno, J. Shi, Mott relation for anomalous Hall and Nernst effects in Ga_(1-x)Mn_(x)As ferromagnetic semiconductors. *Phys. Rev. Lett.* **101**, 117208 (2008).
52. K. Hasegawa, M. Mizuguchi, Y. Sakuraba, T. Kamada, T. Kojima, T. Kubota, S. Mizukami, T. Miyazaki, K. Takanashi, Material dependence of anomalous Nernst effect in perpendicularly magnetized ordered-alloy thin films. *Appl. Phys. Lett.* **106**, 252405 (2015).
53. C. Fang, C. H. Wan, Z. H. Yuan, L. Huang, X. Zhang, H. Wu, Q. T. Zhang, X. F. Han, Scaling relation between anomalous Nernst and Hall effect in Pt/Co (n) multilayers. *Phys. Rev. B* **93**, 054420 (2016).
54. T. Zhu, P. Chen, Q. H. Zhang, R. C. Yu, B. G. Liu, Giant linear anomalous Hall effect in the perpendicular CoFeB thin films. *Appl. Phys. Lett.* **104**, 202404 (2014).
55. L. Q. Liu, C. T. Chen, J. Z. Sun, Spin Hall effect tunnelling spectroscopy. *Nat. Phys.* **10**, 561 (2014).
56. D. Z. Hou, Z. Y. Qiu, R. Iguchi, K. Sato, E. K. Vehstedt, K. Uchida, G. E. W. Bauer, E. Saitoh, Observation of temperature-gradient-induced magnetization. *Nat. Commun.* **7**, 12265 (2016).
57. J. Torrejon, J. Kim, J. Sinha, S. Mitani, M. Hayashi, M. Yamanouchi, H. Ohno, Interface control of the magnetic chirality in CoFeB/MgO heterostructures with heavy-metal underlayers. *Nat. Commun.* **5**, 4655 (2014).
58. J. Kim, J. Sinha, M. Hayashi, M. Yamanouchi, S. Fukami, T. Suzuki, S. Mitani, H. Ohno, Layer thickness dependence of the current induced effective field vector in Ta|CoFeB|MgO. *Nat. Mater.* **12**, 240 (2013).
59. K. Garello, I. M. Miron, C. O. Avci, F. Freimuth, Y. Mokrousov, S. Blugel, S. Auffret, O. Boulle, G. Gaudin, P. Gambardella, Symmetry and magnitude of spin-orbit torques in ferromagnetic heterostructures. *Nat. Nanotechnol.* **8**, 587 (2013).

60. C.-F. Pai, Y. Ou, L. H. Vilela-Leao, D. C. Ralph, R. A. Buhrman, Dependence of the efficiency of spin Hall torque on the transparency of Pt/ferromagnetic layer interfaces. *Phys. Rev. B* **92**, 064426 (2015).
61. A. Brataas, G. E. W. Bauer, P. J. Kelly, Non-collinear magnetoelectronics. *Phys. Rep.* **427**, 157 (2006).
62. Z. B. Guo, W. B. Mi, R. O. Aboljadayel, B. Zhang, Q. Zhang, P. G. Barba, A. Manchon, X. X. Zhang, Effects of surface and interface scattering on anomalous Hall effect in Co/Pd multilayers. *Phys. Rev. B* **86**, 104433 (2012).
63. V. Keskin, B. Aktas, J. Schmalhorst, G. Reiss, H. Zhang, J. Weischenberg, Y. Mokrousov, Temperature and Co thickness dependent sign change of the anomalous Hall effect in Co/Pd multilayers: An experimental and theoretical study. *Appl. Phys. Lett.* **102**, 022416 (2013).

Acknowledgements:

The authors thank S. Bosu and S. S-L. Zhang for fruitful discussions. This work was partly supported by JSPS Grant-in-Aid (15H05702), Casio Foundation, MEXT R & D Next-Generation Information Technology and the Spintronics Research Network of Japan. YCL is an International Research Fellow of the Japan Society for the Promotion of Science.

Author Contributions

M.H. and Y.S. planned the study. P.S. and Y.L. carried out microfabrication, P.S., Y.L. and Y.S. measured the samples and analyzed the results with help of S.M. and M.H. S.T. developed the drift diffusion model. All authors discussed the data and commented on the manuscript.

Competing interests

The authors declare that they have no competing interests.

Data and materials availability

All data needed to evaluate the conclusions in the paper are present in the paper and/or the Supplementary Materials. Additional data related to this paper may be requested from the authors.

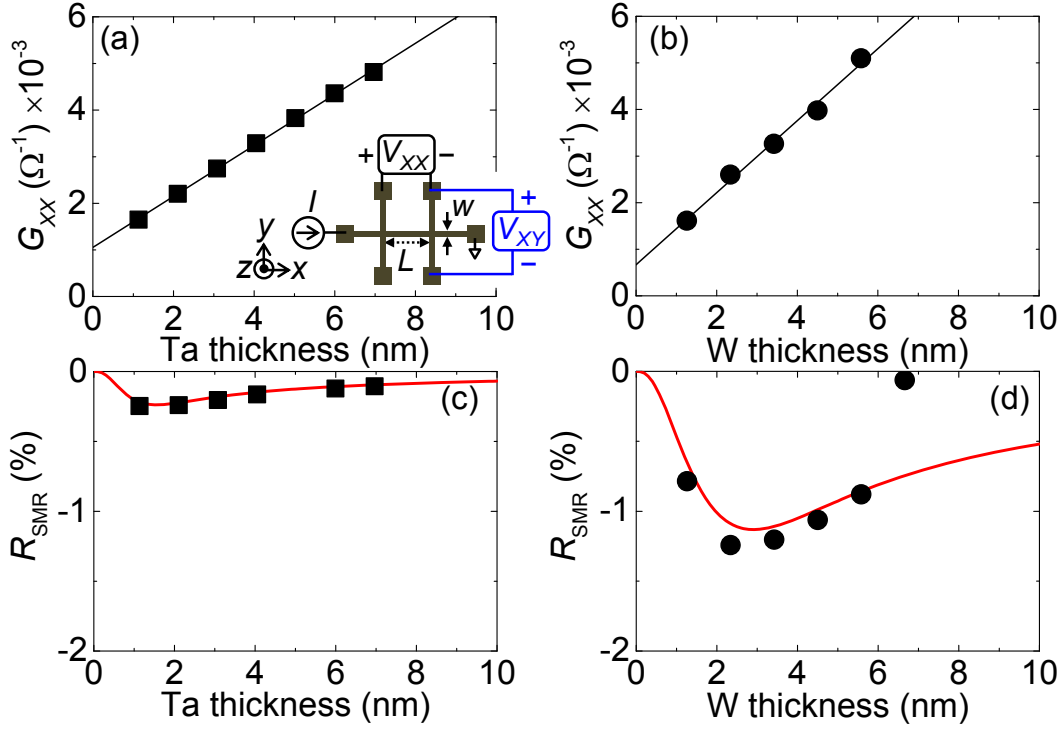


Fig. 1. Longitudinal resistance and SMR of HM|CoFeB|MgO heterostructures. (a,b) Sheet conductance $G_{xx}=L/(wR_{xx})$ vs. HM layer thickness d_N for the Ta (a) and W (b) underlayer films. The solid lines show linear fit to the data in appropriate range of d_N . Schematic of the measurement setup is illustrated in the inset of (a). The inset of (b) is the expanded y-axis plot of the main panel. (c,d) Spin Hall magnetoresistance $R_{SMR}=\Delta R_{xx}/R_{xx}^Z$ plotted against d_N for the Ta (c) and W (d) underlayer films. The red solid lines are fit to the data using Eq. (1). Parameters used in the fitting are summarized in Table 1.

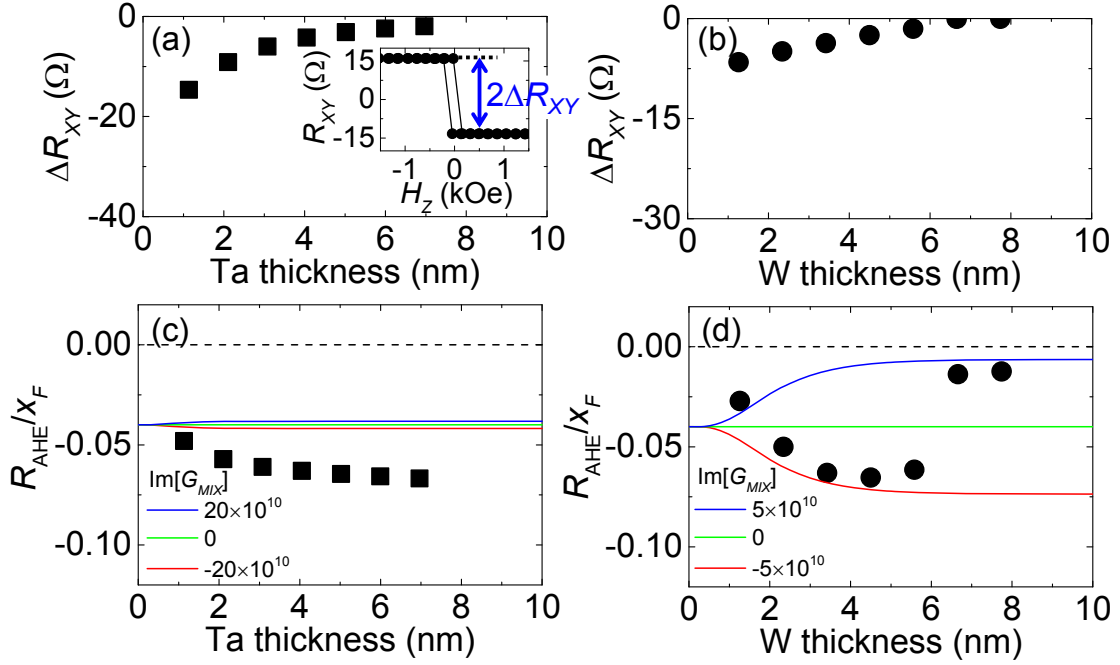


Fig. 2. HM layer thickness dependence of the anomalous Hall resistance. (a,b) The HM layer thickness d_N dependence of the anomalous Hall resistance ΔR_{XY} for the Ta (a) and W (b) underlayer films. The inset of (a) shows R_{XY} vs. H_Z for sub. |~1.1 Ta| 1 CoFeB|2 MgO|1 Ta (thickness in nm). Definition of ΔR_{XY} is schematically illustrated. (c,d) The normalized anomalous Hall coefficient $R_{AHE}/x_F = (\Delta R_{XY} L) / (w R_{XX}^Z x_F)$ plotted against d_N for Ta (c) and W (d) underlayer films. The solid lines show fit to the data using Eq. (2) with three different values of $\text{Im}[G_{MIX}]$. Parameters used in the fitting are summarized in Table 1 except for $\text{Im}[G_{MIX}]$ noted in the legend.

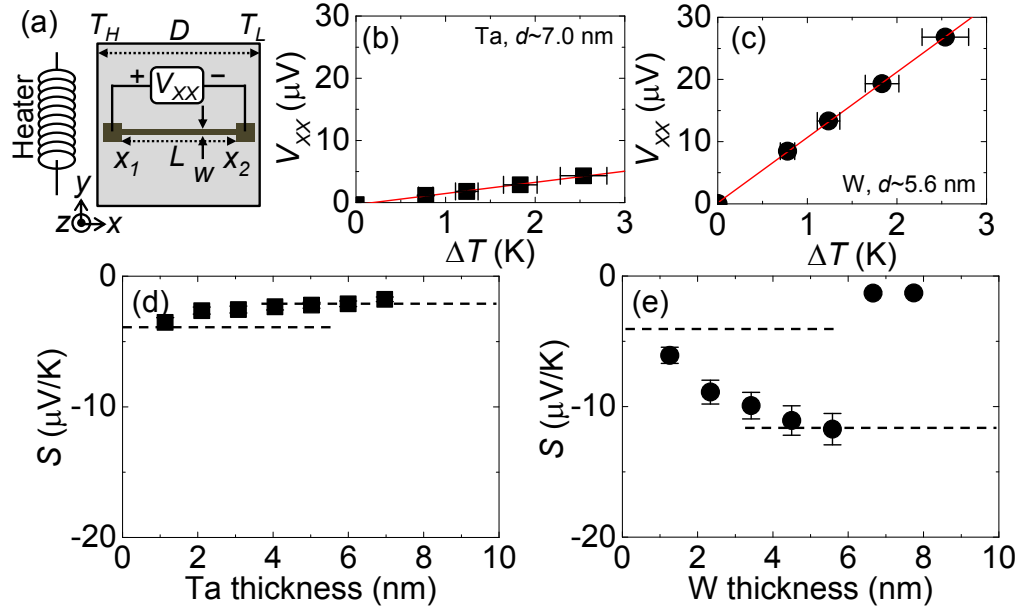


Fig. 3. Seebeck coefficient of HM|CoFeB|MgO heterostructures. (a) Schematic illustration of the measurement setup for temperature gradient induced longitudinal voltage. The bright square represents part of the substrate; the dark region indicates the area where the device is located. $D=0.7$ cm, $L=0.6$ cm, $w=50$ μm . (b,c) The longitudinal (Seebeck) voltage V_{xx} measured as a function of the temperature difference ΔT for sub. $|\sim 7.0$ Ta|1 CoFeB|2 MgO|1 Ta (b) and sub. $|\sim 5.6$ W|1 CoFeB|2 MgO|1 Ta (c). The horizontal and vertical error bars represent, respectively, the uncertainty of the temperature gradient and the variation of the voltage under a fixed temperature gradient. (d,e) The Seebeck coefficient $S = -(V_{xx}/L)/(\Delta T/D)$ plotted against d_N for Ta (d) and W (e) underlayer films. The error bars denote the variation of S due to the uncertainty of the temperature gradient. The horizontal dashed lines are guide to the eye which provide estimate of the Seebeck coefficient of the HM and FM layers.

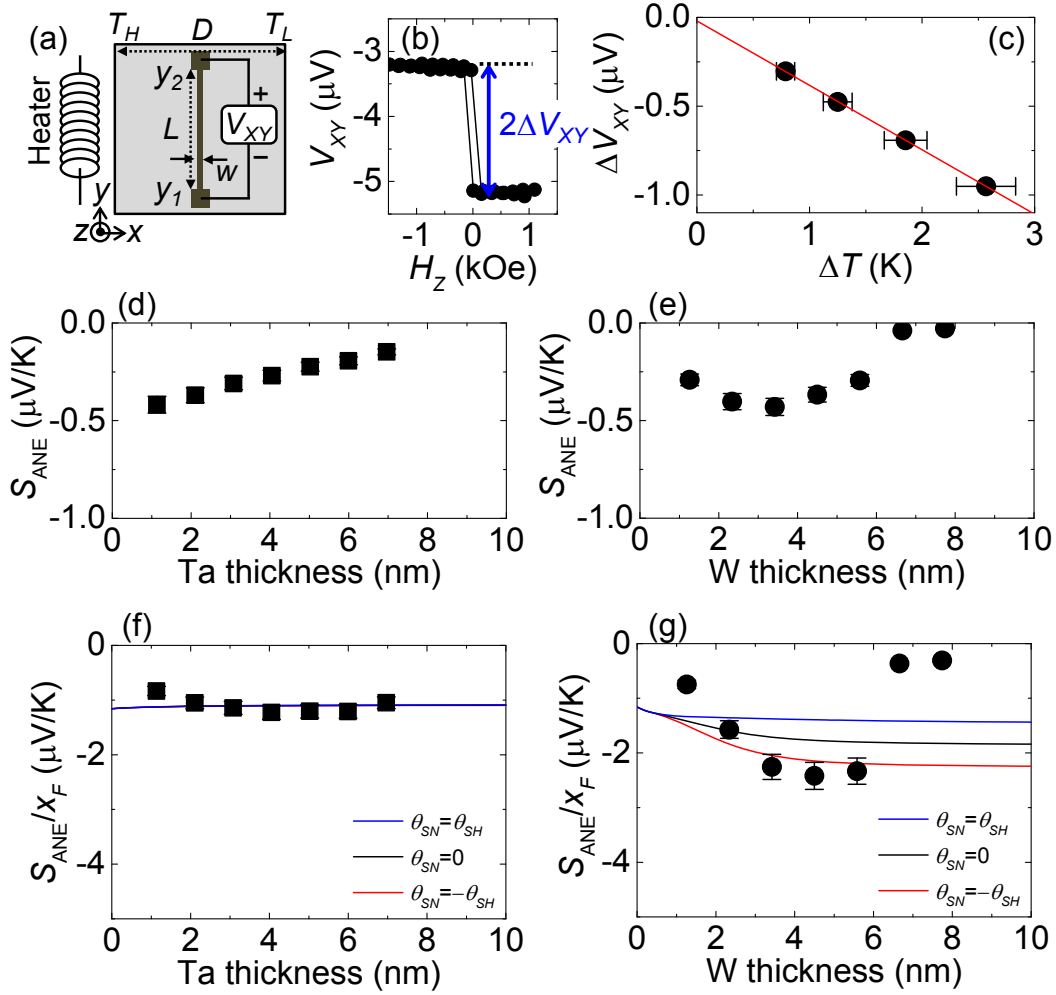


Fig. 4. HM layer thickness dependence of the anomalous Nernst effect. (a) Schematic illustration of the measurement setup for temperature gradient induced transverse voltage. The bright square represents part of the substrate; the dark region indicates the area where the device is located. $D=0.7$ cm, $L=0.6$ cm, $w=50$ μm . (b) The transverse voltage V_{XY} vs. H_z of sub. | ~ 3.4 W| 1 CoFeB| 2 MgO| 1 Ta when a temperature difference of $\Delta T \sim 2.5$ K is applied. The definition of ΔV_{XY} is schematically drawn by the blue arrow. (c) ΔT dependence of the anomalous Nernst voltage ΔV_{XY} for the same sample described in (b). The horizontal and vertical error bars represent, respectively, the uncertainty of the temperature gradient and the variation of the voltage under a fixed temperature gradient. The red solid line shows linear fit to the data. (d,e) Anomalous Nernst coefficient $S_{\text{ANE}} = (\Delta V_{XY}/L)/(\Delta T/D)$ plotted against d_N for the Ta (d) and W (e) underlayer films. (f,g) d_N dependence of the normalized anomalous Nernst coefficient $S_{\text{ANE}}/x_F = (\Delta V_{XY} D)/(L \Delta T x_F)$ for the Ta (f) and W (g) underlayer films. The error bars in (d-g) denote the variation of quantities due to the uncertainty of the temperature gradient. The solid lines in (f,g) show fit to the data using Eq. (6) with three different values of θ_{SN} . Parameters used in the fitting are summarized in Table 1.

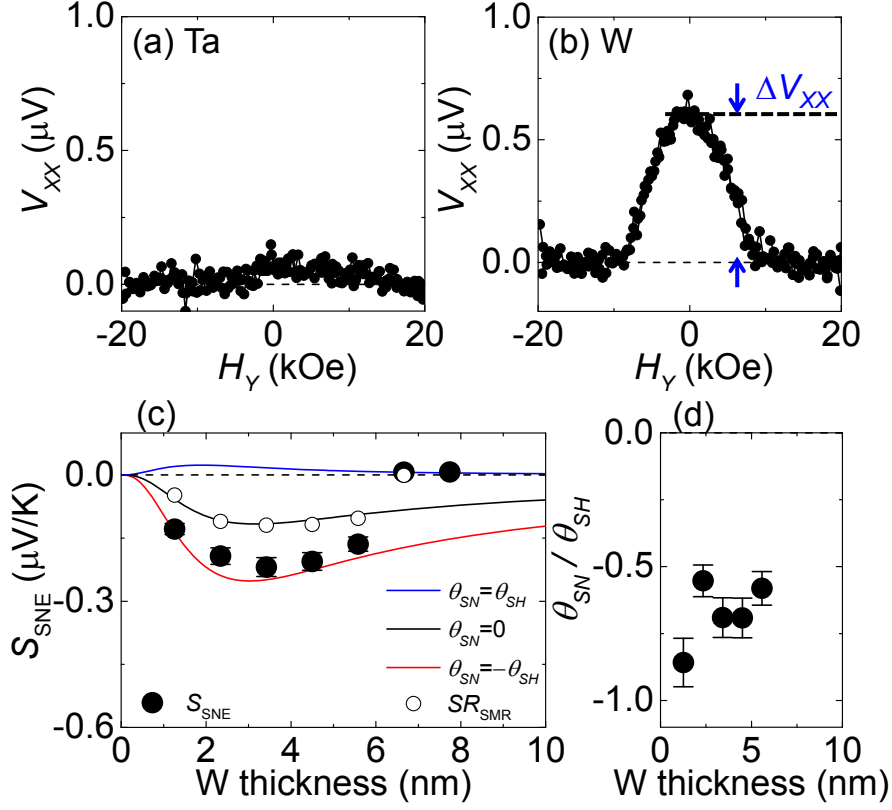


Fig. 5. Signatures of the spin Nernst magnetoresistance. (a,b) The longitudinal (Seebeck) voltage V_{XX} vs. H_Y for sub. $_{\sim 3.1}$ Ta|1 CoFeB|2 MgO|1 Ta (a) and sub. $_{\sim 3.4}$ W|1 CoFeB|2 MgO|1 Ta (b) when a temperature difference of $\Delta T \sim 3.5$ K is applied. The definition of ΔV_{XX} is schematically drawn. (c) d_N dependence of spin Nernst magnetoresistance $S_{SNE} = (\Delta V_{XX}/L)/(\Delta T/D)$ (solid circles) and the scaled spin Hall magnetoresistance SR_{SMR} (open circles) for the W underlayer films. The solid lines show calculated S_{SNE} using Eq. (5) with three different values of θ_{SN} . Parameters used in the fitting are summarized in Table 1. (d) d_N dependence of θ_{SN}/θ_{SH} obtained from $S_{SNE}/(SR_{SMR})$ and the relation described in Eq. (7). The error bars in (c) and (d) denote the variation of quantities due to the uncertainty of the temperature gradient.

Table 1. Parameters used to describe the experimental results. Resistivity (ρ_N), Seebeck coefficient (S_N), spin diffusion length (λ_N), spin Hall angle (θ_{SH}), spin Nernst angle (θ_{SN}) of the heavy metal (HM) layer, and resistivity (ρ_F), Seebeck coefficient (S_F), anomalous Hall angle (θ_{AH}), anomalous Nernst angle (θ_{AN}) of the ferromagnetic metal (FM) layer in HM/FM/MgO heterostructure. $\text{Re}[G_{MIX}]$ and $\text{Im}[G_{MIX}]$ represent the real and imaginary parts of the spin mixing conductance G_{MIX} at the HM/FM interface.

Film structure	HM layer					F layer				Interface	
	ρ_N $\mu\Omega\text{cm}$	S_N $\mu\text{V/K}$	λ_N nm	θ_{SH}	θ_{SN}	ρ_F $\mu\Omega\text{cm}$	S_F $\mu\text{V/K}$	θ_{AH}	θ_{AN}	$\text{Re}[G_{MIX}]$ $\Omega^{-1}\text{cm}^{-2}$	$\text{Im}[G_{MIX}]$ $\Omega^{-1}\text{cm}^{-2}$
Ta/CoFeB	183	-2	0.5	-0.13	N/A	160	-4	0.04	-0.25	2×10^{10}	-20×10^{10}
W/CoFeB	130	-12	1.1	-0.28	varied						-5×10^{10}

Supplementary Material

The spin Nernst effect in Tungsten

Peng Sheng¹, Yuya Sakuraba¹, Yong-Chang Lau^{1,2}, Saburo Takahashi³, Seiji Mitani¹ and Masamitsu Hayashi^{1,2*}

¹*National Institute for Materials Science, Tsukuba 305-0047, Japan*

²*Department of Physics, The University of Tokyo, Bunkyo, Tokyo 113-0033, Japan*

³*Institute for Materials Research, Tohoku University, Sendai 980-8577, Japan*

1. Additional experimental results

Magnetic properties of the heterostructures

The magnetic properties of the heterostructures are evaluated using vibrating sample magnetometry. The results are presented in Fig. S1.

Plots of Spin Nernst magnetoresistance

The temperature gradient induced longitudinal voltage V_{XX} is plotted as a function of magnetic field applied along the y-axis in Figs. S2(a-i) for the Ta (a,b) and W (c-i) underlayer films. V_{XX} vs. H_X and H_Z for the W underlayer films are plotted in Figs. S2(j-m). The thickness of the HM layer (Ta or W) is listed in the legend. The applied temperature gradient ΔT is ~ 3.5 K.

Thermoelectric properties of CoFeB

To study contribution from the CoFeB layer on the spin transport properties of the Sub./HM/CoFeB/MgO/cap heterostructures, films without the heavy metal (HM) layer, i.e. Sub./CoFeB/MgO/cap heterostructures are studied. From hereafter, we refer to the latter heterostructure as "CoFeB films". The results are summarized in Figs. S3 and S4.

The CoFeB thickness dependence of the sheet conductance (G_{XX}) is plotted in Fig. S4(a). The resistance increases abruptly as the thickness (t_F) of the CoFeB layer is reduced to near ~ 1 nm. Below $t_F \sim 1$ nm, the device resistance cannot be evaluated. Note that for film structures with the HM underlayer, the resistance of devices with $t_F \sim 1$ nm is significantly smaller. We consider such difference arises due to change in the film growth mode. The HM layer serves as a good seed layer for growing films on SiO_x surfaces; Ta is a good example that is well known and widely used. Without the HM layer, the growth mode of CoFeB changes from layer growth to island growth. For thin CoFeB films ($t_F \lesssim 1$ nm) without the HM layer, the film morphology may not be uniform and continuous. For these reasons, studies of the CoFeB films without the HM underlayer are limited to thicknesses (t_F) larger than ~ 1 nm.

From the in-plane field (H_Y) dependence of the longitudinal resistance (R_{XX}), we find the spin Hall magnetoresistance (SMR) of the CoFeB films to be $\sim -0.01\%$ to $\sim 0.1\%$ (Figs. S3a-d). The CoFeB thickness dependence of the SMR ($R_{\text{SMR}} = \Delta R_{XX} / R_{XX}^Z$) is plotted in Fig. S4(b). Since the signal is small, it is not clear what is causing the positive SMR for the thinner CoFeB films: the resistance measurements may capture effects other than

SMR (e.g. anisotropic magnetoresistance related to interface states). However, the magnitude of the SMR found in the CoFeB films is one order of magnitude smaller than that of Ta underlayer films and nearly two orders of magnitude smaller than that of the W underlayer films.

The out of plane field (H_z) dependence of the anomalous Hall resistance and the anomalous Nernst voltage are plotted in Figs. S3(e-j). The normalized anomalous Hall coefficient $R_{\text{AHE}}/x_F = (\Delta R_{XY}L)/(R_{XX}^Z w x_F)$ and the normalized anomalous Nernst coefficient $S_{\text{ANE}}/x_F = (\Delta V_{XY}D)/(\Delta T L x_F)$ of the CoFeB films are plotted as a function of its thickness (t_F) in Figs. S4(c) and S4(f), respectively. These results are compared to the results of heterostructures with the HM layer (Figs. S4(d,e) and S4(g,h)). We find that the small HM layer thickness (d_N) limit of R_{AHE}/x_F and S_{ANE}/x_F more or less agree with that of the thick CoFeB films. As the thicker CoFeB films are likely more uniform than its thinner counterpart, it may be reasonable to compare results from the thicker CoFeB films with those of the small d_N limit of films with the HM underlayer. Note that when fitting S_{ANE}/x_F with Eq. (6), we use a value of θ_{AN} that results in a larger S_{ANE}/x_F than that of the CoFeB films. In order to describe all results (R_{SMR} , R_{AHE}/x_F , S_{ANE}/x_F and S_{SNE}) with a single parameter set, θ_{AN} needs to take a value slightly larger than what is expected for CoFeB films without the HM layer.

The Seebeck coefficient $S = -(V_{XX}/L)/(\Delta T/D)$ of the CoFeB films are compared to that of the HM layer included heterostructures in Fig. S4(i-k). The Seebeck coefficient of the CoFeB films shows little dependence on the CoFeB thickness (Fig. S4(i)). The small d_N limit of S is consistent with that of the CoFeB films.

Finally, the temperature gradient induced longitudinal voltage (V_{xx}) of the CoFeB films is plotted as a function of H_Y in Figs. S3(k-n). For the thicker CoFeB films, we find signals which resemble that of the anomalous Nernst effect (ANE), i.e. the level of V_{xx} is different for positive and negative H_Y . It should be noted that the CoFeB films used here has easy plane anisotropy, different from the heterostructures with the HM underlayer that possess uniaxial perpendicular magnetic anisotropy. We consider the ANE like signal appears due to an unintended out of plane temperature gradient applied across the film. Influence of such out of plane temperature gradient on the thermoelectric measurements has been pointed by previous reports(15, 43-45). However, it should be noted that the ANE-like signal decreases with decreasing CoFeB thickness, consistent with previous report(43).

As the CoFeB layer thickness is reduced, the noise level of V_{xx} tends to increase (see Figs. S3(k-n)). We consider such increase in the noise level is related to the film morphology and the resistance of the CoFeB layer: thinner CoFeB layers are less likely to form a continuous layer and thus the resistance considerably increases, giving rise to large Johnson noise. However, in the thicker CoFeB films with smaller noise level (Figs. S3(k-n)), we find almost no signal that resembles that of the H_Y dependence of V_{xx} shown in Fig. 5(b).

Magnitude of the unintended out of plane temperature gradient

We can estimate the magnitude of the unintended out of plane temperature gradient found in the samples shown in Figs. S3(m) and S3(n) using the corresponding ANE

measurements: see Figs. S3(i) and S3(j). Comparing the voltage difference when the magnetization direction is reversed, we estimate the out of plane temperature gradient to be $\sim 15\%$ ($\sim 23\%$) of the in-plane temperature gradient for the samples with CoFeB thickness of ~ 1.9 nm (~ 2.2 nm). The results presented in Figs. S3(k,l,m,n) show that the out of plane temperature gradient and consequently the ANE-like signal tend to decrease as the CoFeB layer thickness is reduced. This is in accordance with previous report, which concluded that an unintended out of plane temperature gradient increases with increasing thickness of the magnetic layer due to the difference in the thermal conductivity of the substrate and the film(43). As the thickness of the CoFeB layer ($t_F \sim 1$ nm) used for the studies presented in Figs. 1-5 are thinner than those shown in Fig. S3 and S4, we consider the effect of the unintended out of plane temperature gradient on the longitudinal voltage in the W underlayer films is negligible.

2. Discussion related to other effects that may influence the voltage measurements

Spin Seebeck effect

Here we discuss the effect of the spin Seebeck effect(9, 12) on the voltage measurements. First we consider the influence of the unintended out of plane temperature gradient (along z in Figs. 3(a) and 4(a)).

For the anomalous Nernst effect measurements, the transverse voltage (V_{XY}) is measured against the out of plane field (H_Z). In this experimental setting, the magnetization of the FM layer always points along the film normal. With an unintended out of plane temperature gradient, the spin Seebeck effect within the FM layer will

generate, if any, spin current with both spin (σ) and flow (J_S) pointing along the film normal (along z). The inverse spin Hall effect (ISHE) will not generate any voltage (V_{XY}) in the HM layer since the charge current J is proportional to the cross product of σ and J_S , i.e. $J \propto J_S \times \sigma$. Thus we expect no contribution from the ISHE on the transverse voltage measurements with the unintended out of plane temperature gradient (this condition corresponds to the cartoon of Table S1, row D, column "Setup 2").

Next, we consider the influence of the spin Seebeck effect and the ISHE on V_{XX} (with the unintended out of plane temperature gradient). Note that for the spin Nernst coefficients measurements, we compare the difference of V_{XX} when the magnetization of the FM layer is pointing along the film normal (z -axis) and along the film plane (y -axis). V_{XX} is expected to be zero when the magnetization is pointing along the film normal since the directions of both spin and flow of the spin current, if any, are parallel ($J_S \parallel e_z$, $\sigma \parallel e_z$). When the magnetization is rotated toward the y -axis, there is a possibility that the spin Seebeck effect and the ISHE generate a longitudinal voltage. Under such circumstance, H_Y will dictate the spin direction (σ) of the spin current and thus V_{XX} changes its sign when the magnetization direction is reversed along the y -axis due to the ISHE (e.g. $J_S \parallel e_z$, $\sigma \parallel \pm e_y$, $J \propto J_S \times \sigma \sim \mp e_x$); see cartoon of Table S1, row D, column "Setup 1". In our experiments, we do not observe such difference in V_{XX} when the magnetization is reversed between $+y$ and $-y$ (see Fig. 5(b) and Figs. S2(c-g)). We thus consider such contribution from the unintended out of plane temperature gradient, spin Seebeck effect and ISHE is negligible in the spin Nernst coefficient measurements.

With the in-plane temperature gradient (applied along x as in Figs. 3(a) and 4(a)), the spin Seebeck effect and the ISHE can generate a non-zero V_{XX} at the hot and cold ends of the heterostructures under application of H_Y . However, since V_{XX} at the hot and cold ends are opposite (e.g. due to the diffusion of accumulated spins, $\mathbf{J}_S \parallel \mathbf{e}_z$ for the hot end and $\mathbf{J}_S \parallel -\mathbf{e}_z$ for the cold end; $\boldsymbol{\sigma} \parallel \pm \mathbf{e}_y$ is determined by H_Y , thus $\mathbf{J} \propto \mathbf{J}_S \times \boldsymbol{\sigma} \sim \mp \mathbf{e}_x$ for the hot and $\mathbf{J} \sim \pm \mathbf{e}_x$ for the cold end), they will cancel out and result in a net zero V_{XX} (Table S1, row C, column "Setup 1"). The transverse voltage V_{XY} vs. H_Z is also expected to be zero since the spin accumulation ($\boldsymbol{\sigma}$) due to the spin Seebeck effect at the edges will not generate any V_{XY} due to the ISHE ($\boldsymbol{\sigma}$ and \mathbf{J}_S are both along z). This is shown in Table S1, row C, column "Setup 2".

Anomalous Nernst effect

Here we consider the influence of the anomalous Nernst effect together with the unintended out of plane temperature gradient (along z in Figs. 3(a) and 4(a)). The transverse charge current due to the ANE is: $\mathbf{J} \propto \nabla T \times \mathbf{M}$. Under application of H_Z , V_{XX} and V_{XY} are expected to be zero since the magnetization (\mathbf{M}) and the temperature gradient (∇T) are parallel. Thus V_{XY} vs. H_Z is expected to be flat, as shown in Table S1, row E, column "Setup 2".

The in-plane field (H_Y) dependence of V_{XX} will show different voltage levels at $+H_Y$ and $-H_Y$ since \mathbf{M} is determined by H_Y (e.g. $\nabla T \parallel \mathbf{e}_z$, $\mathbf{M} \parallel \pm \mathbf{e}_y$, $\mathbf{J} \propto \nabla T \times \mathbf{M} \sim \mp \mathbf{e}_x$).

Table S1, row E, column "Setup 1" shows a cartoon that one would expect for this configuration.

In all cases, the expected curves are different from the experimental results shown in the main text. We thus consider the anomalous Nernst effect driven by an unintended out of plane temperature gradient has little influence on the measurements we performed.

Spin Hall and spin Nernst effect of the FM layer

The spin Hall and spin Nernst effects of the FM (CoFeB) layer contribute to the measured voltage in a similar way as the two effects of the HM layer do (see cartoons of Table S1, row F, columns "Setup 1" and "Setup 2"). Although the size of the spin Hall angle of ferromagnetic materials is an issue currently debated, reports up to date show that the effect is much smaller than that of the heavy metal layers(46-48). For example, the spin Hall angle of Py has been reported to be $\sim 0.005-0.013$ (refs. (46, 47)), significantly smaller than that of Ta (~ 0.13) and W (~ 0.28).

Contribution from the spin Hall/spin Nernst effects of the FM layer on the spin transport properties of the HM/FM bilayer can be included in the model and we find that the ratio θ_{SN}/θ_{SH} is not significantly influenced with moderate values (smaller than ~ 0.1) of θ_{SN} and θ_{SH} of the FM layer. Details of the model calculations will be presented elsewhere. We thus consider obtaining θ_{SN}/θ_{SH} from the experimental results (Figs. 1(d), 3(e), 5(c)) provides a robust way to estimate the spin Nernst effect of non-magnetic materials.

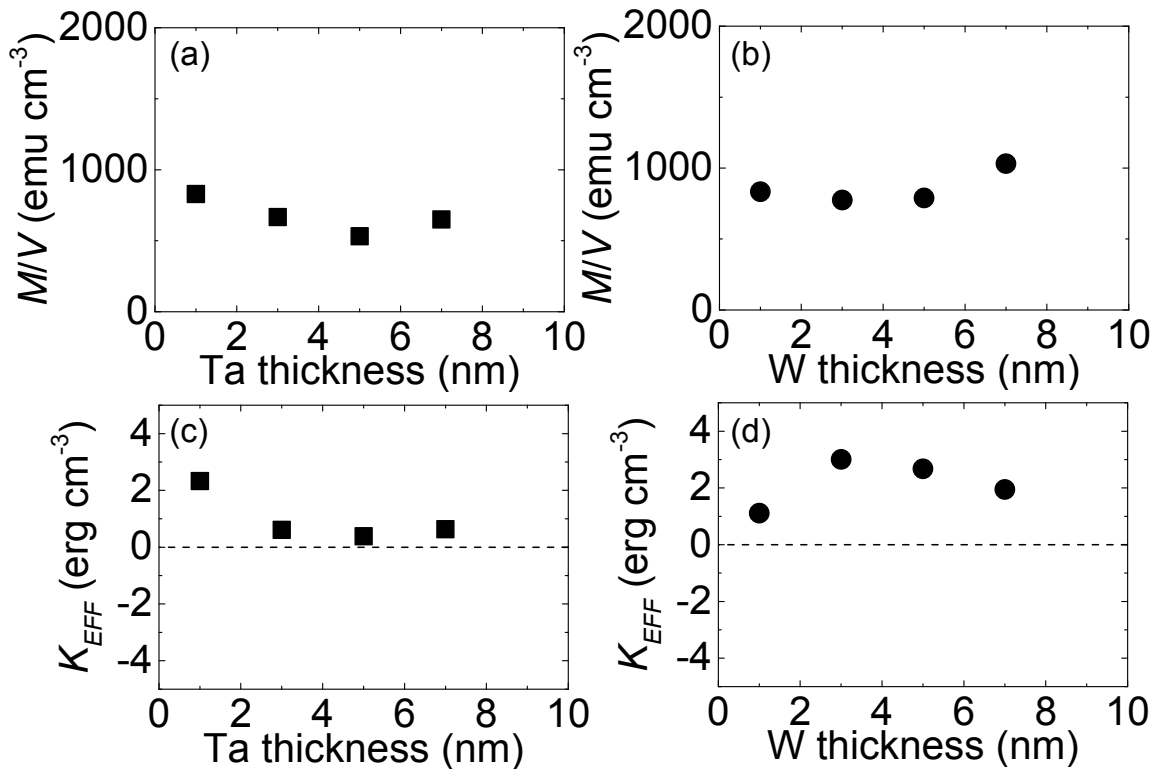


Fig. S1. Magnetic properties of HM|CoFeB|MgO heterostructures. (a-d) Saturated magnetic moments per unit volume M/V (a,b) and effective magnetic anisotropy energy K_{EFF} (c,d) plotted as a function of the HM layer thickness d_N for Ta (a,c) and W (b,d) underlayer films.

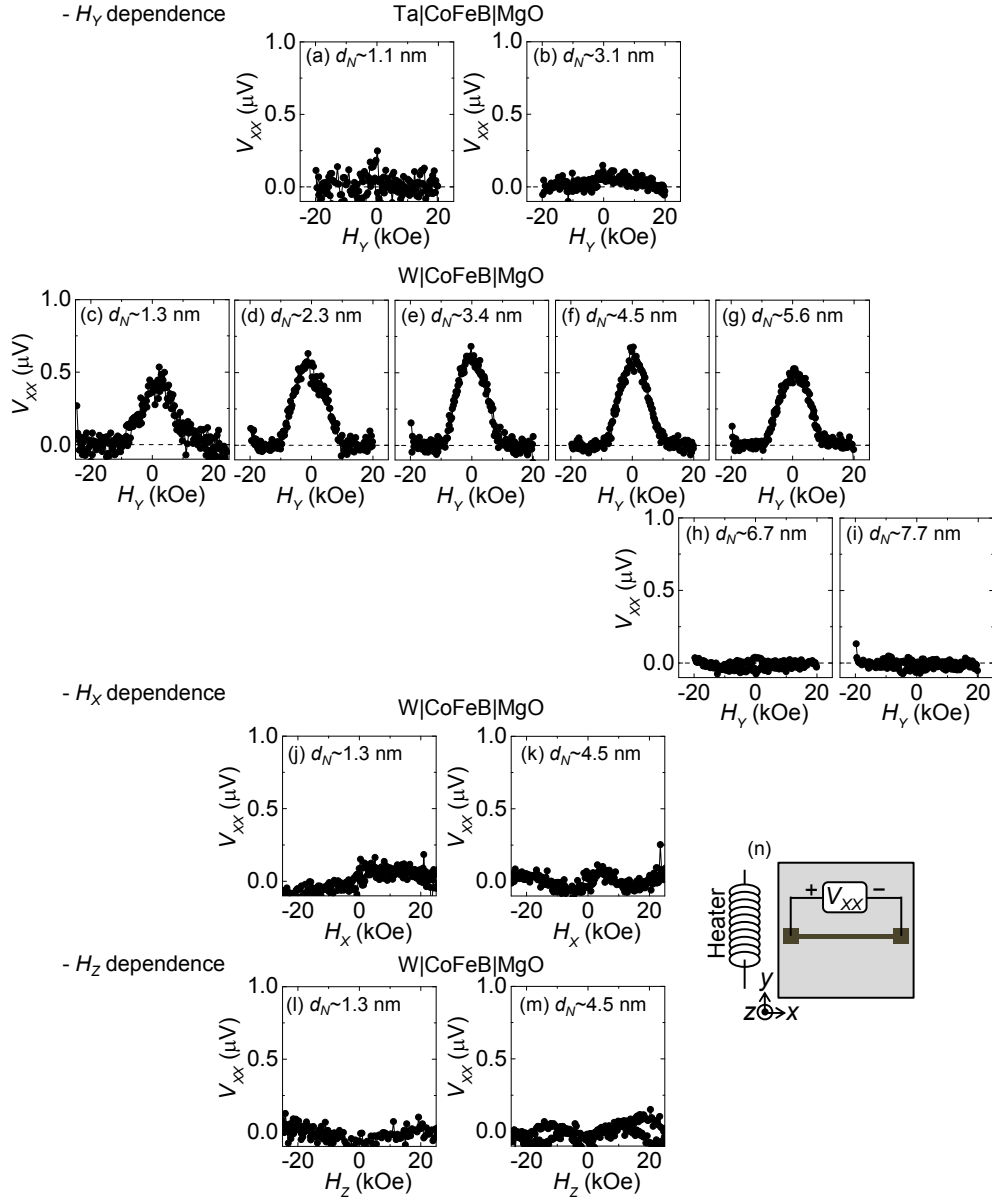


Fig. S2. Spin Nernst magnetoresistance of Ta and W underlayer films. (a-h) The longitudinal (Seebeck) voltage V_{XX} vs. H_Y of the Ta underlayer films (a,b) and the W underlayer films (c-i). (j-m) H_X and H_Z dependence of V_{XX} for the W underlayer films. A temperature difference $\Delta T \sim 3.5$ K is applied across part of the substrate ($D \sim 7$ mm). d_N denotes the thickness of the HM (Ta or W) underlayer. (n) Schematic of the experimental setup and the coordinate axis.

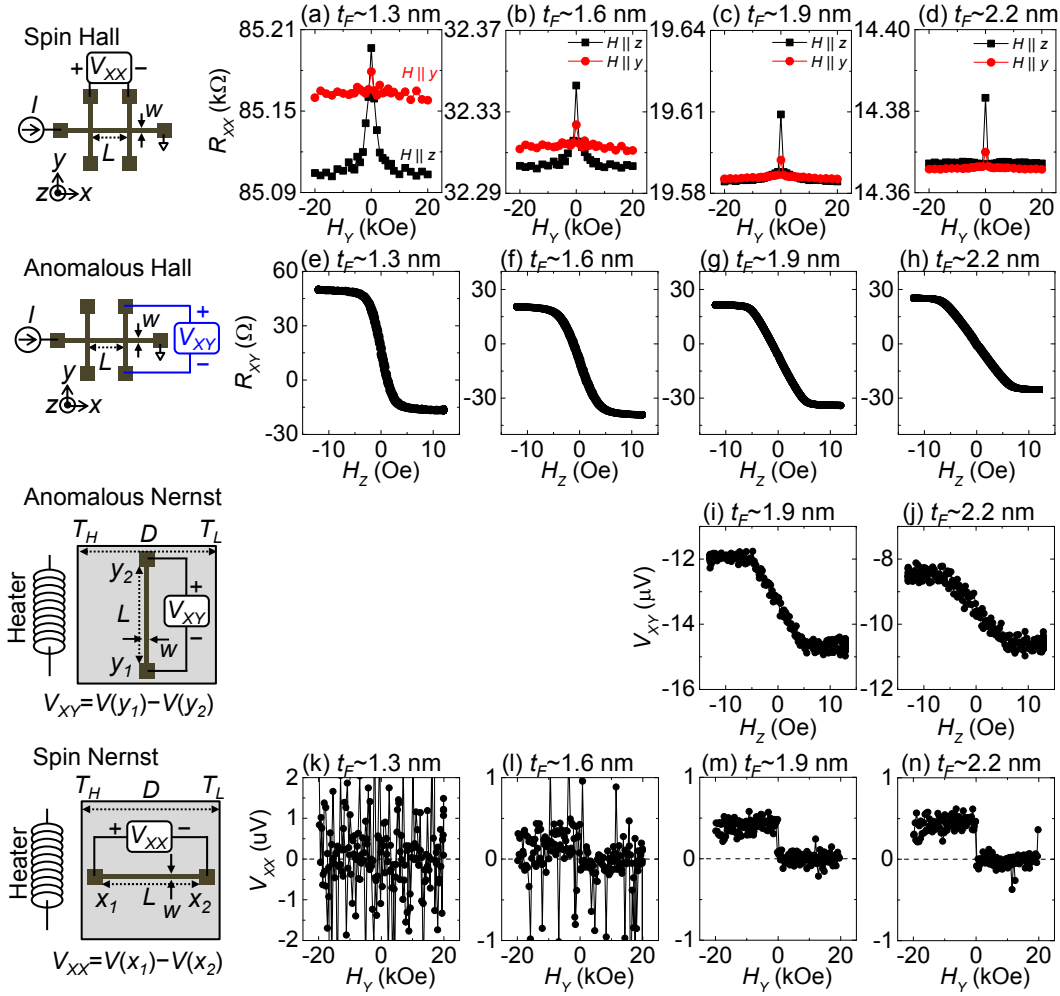


Fig. S3. Thermoelectric properties of CoFeB thin films without the HM layer. (a-n) In plane field (H_y) dependence of the longitudinal resistance R_{XX} (a-d), out of plane field (H_z) dependence of the transverse resistance R_{XY} (e-h), H_z dependence of the temperature gradient induced transverse voltage V_{XY} (i,j) and H_y dependence of the temperature gradient induced longitudinal voltage V_{XX} (k-n) for sub- $|t_F$ CoFeB|2 MgO|1 Ta (thickness in nm) heterostructures. The thickness of the CoFeB layer (t_F) is listed on top of each panel. Schematics of the experimental setup are displayed on the left. For (i-n), the applied temperature gradient ΔT is ~ 3.5 K. The longitudinal voltages V_{XX} shown in (k-n) are vertically shifted so that the large H_y limit of V_{XX} becomes zero.

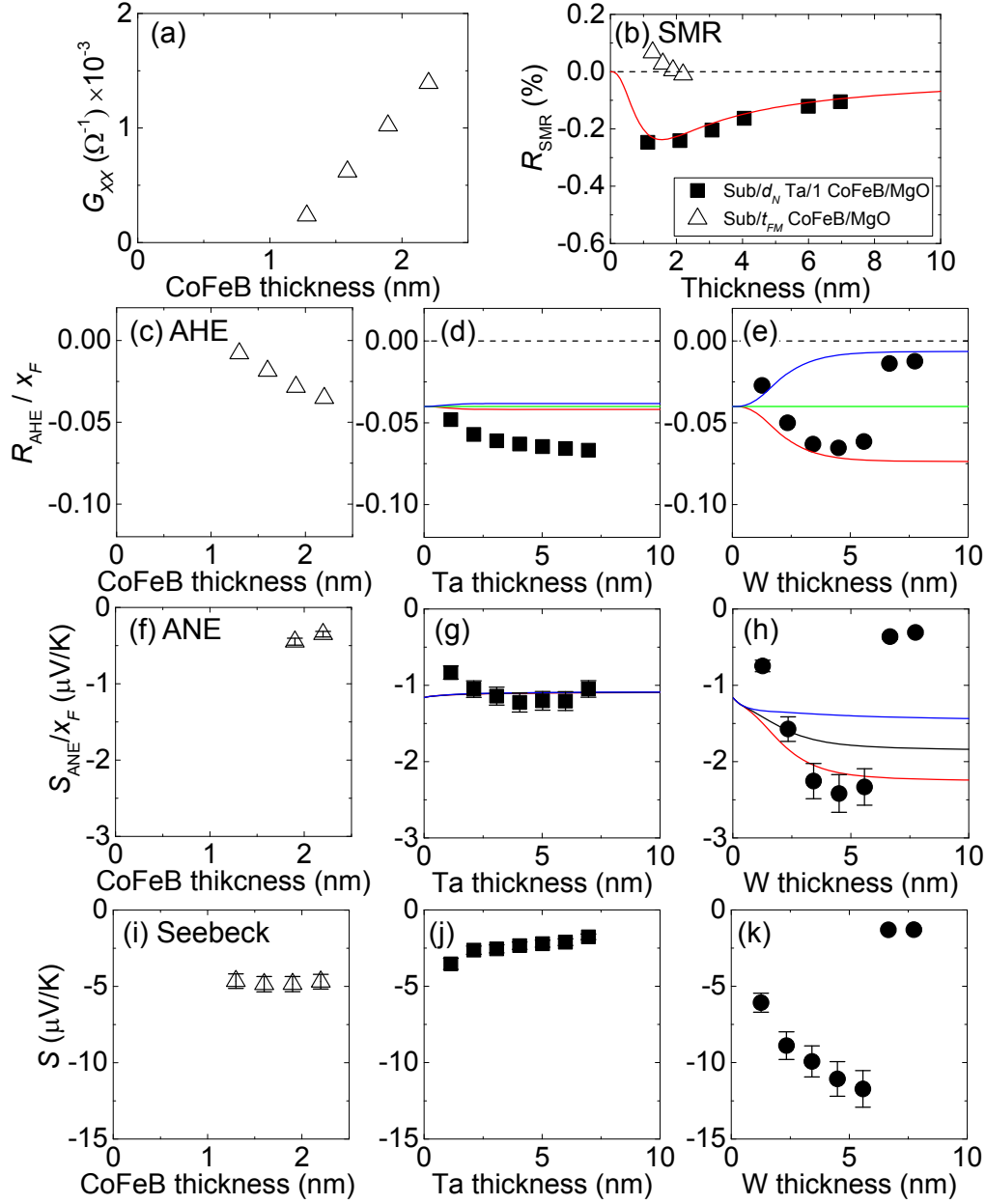


Fig. S4. Comparison of parameters with and without the HM layer. (a,b) CoFeB thickness dependence of the sheet conductance $G_{XX}=L/(wR_{XX})$ (a) and the spin Hall magnetoresistance $R_{SMR}=\Delta R_{XX}/R_{XX}^Z$ (b). R_{SMR} for the Ta underlayer films are shown as a reference. (c-e) Normalized anomalous Hall coefficient $R_{AHE}/x_F=(\Delta R_{XY}L)/(R_{XX}^Z wx_F)$ plotted against CoFeB (c), Ta (d) and W (e) layer thicknesses. (f-h) CoFeB (f), Ta (g) and W (h) layer thicknesses dependence of the normalized anomalous Nernst coefficient $S_{ANE}/x_F=(\Delta V_{XY}D)/(\Delta TLx_F)$. (i-k) Seebeck coefficient $S=-(V_{XX}/L)/(\Delta T/D)$ plotted as a function of CoFeB (i), Ta (j) and W (k) layer thicknesses. The error bars in (f-k) denote variation of quantities due to the uncertainty of the temperature gradient. Film structure used are sub. $|t_F$ CoFeB|2 MgO|1 Ta (a,b,c,f,i), sub. $|d_N$ Ta|1 CoFeB|2 MgO|1 Ta (d,g,j) and sub. $|d_N$ W|1 CoFeB|2 MgO|1 Ta (e,h,k).

Table S1. Influence of other phenomena* on the temperature gradient induced voltage measurements.

		Setup 1 V_{XX} vs. H_Y (Fig.3a)	Setup 2 V_{XY} vs. H_Z (Fig.4a)
Magnetization			
Sources			
A	ΔT along x Spin Nernst (HM) Spin Hall magnetoresistance		
B	ΔT along x Anomalous Nernst (FM)		
C	ΔT along x Spin Seebeck effect (FM) Inverse spin Hall effect (HM)		
D	(Unintended) ΔT along z Spin Seebeck effect (FM) Inverse spin Hall effect (HM)		
E	(Unintended) ΔT along z Anomalous Nernst (FM)		
F	ΔT along x Spin Nernst (FM) Spin Hall magnetoresistance		

*The two columns (“Setup 1“ and “Setup 2“) show the in-plane field (H_Y) and out of plane field (H_Z) dependence of the properties represented by the y-axis title of each panel. The top row show measured M - H loops of sub.[3 W|1 CoFeB|2 MgO|1 Ta. The rows labeled A-F illustrate the expected transverse (V_{XY}) and longitudinal (V_{XX}) voltages when the phenomena indicated in the corresponding left column take place. For example, if an unintended out of plane temperature gradient (ΔT along z) is applied and the spin Seebeck effect occurs in the FM layer together with the inverse spin Hall effect in the HM layer (row D), we expect an asymmetric V_{XX} vs. H_Y and a nearly zero V_{XY} vs. H_Z . For rows A and B, V_{XY} is due to both the spin Nernst and anomalous Nernst effects; the rows are thus merged.